



Pushing the boundaries
of chemistry?
It takes
#HumanChemistry

Make your curiosity and talent as a chemist matter to the world with a specialty chemicals leader. Together, we combine cutting-edge science with engineering expertise to create solutions that answer real-world problems. Find out how our approach to technology creates more opportunities for growth, and see what chemistry can do for you at:

evonik.com/career



Melt-Processing of Complementary Semiconducting Polymer Blends for High Performance Organic Transistors

Yan Zhao, Xikang Zhao, Michael Roders, Aristide Gumyusenge, Alexander L. Ayzner, and Jianguo Mei*

Dedicated to Professor John R. Reynolds on the occasion of his 60th birthday

Semiconducting polymers have attracted enormous interest for their technological relevance in the new generation of flexible and printed electronics.^[1–5] With charge carrier mobilities of organic semiconductors repeatedly surpassing $1 \text{ cm}^2 \text{ V}^{-1} \text{ s}^{-1}$, the main technological hurdle that limits the application of organic circuitry may no longer be the commonly perceived low mobility, but is rather a simple and robust process that can provide excellent device yields with low cost. Solution processing is considered to be a promising technology for organic electronics and has been at the center of thin film formation in organic electronics, presumably because it can potentially deliver low cost, fast roll-to-roll print processing.^[6] However, there are a number of issues that are undermining solution processing as a viable technology for large scale manufacturing, such as the use of chlorinated solvents, the composition instability of organic semiconductor solutions, the formation of kinetically trapped morphologies, and the profound impact of organic solvent residue in thin films, among others.^[7–11]

Melt-processing involves a reversible liquefaction–solidification process. It is broadly used in industry to produce plastic thin films. Arguably, melt-processing is free from all the drawbacks previously mentioned for solution processing, yet nearly all the benefits are preserved. Stingelin-Stutzmann and co-workers have performed extensive studies on melting poly(3-hexylthiophenes) and small molecule organic semiconductors.^[12–15] The adoption of melt-processing for organic electronics is however further complicated by the fact that almost all high performance donor–acceptor-based semiconducting polymers exhibit high melting temperatures (i.e., $>250 \text{ }^\circ\text{C}$) or decompose before they melt. This is because such high performing polymers usually have extended π -conjugation and “torsion-free” planar polymer backbones.^[16] One way to lower melt-processing temperatures is to make semiconducting polymers with characteristically low melting temperatures. This can be achieved by incorporating flexible spacers into the

polymer backbones^[17–22] or by making insulating-semiconducting block copolymers.^[12,13] Unfortunately, such polymers usually show poor electronic performance because of the lack of effective charge transport pathways or the presence of excessive insulating chains.^[18–20] The other way to lower melt-processing temperatures is to physically blend high melting point semiconducting polymers into low melting point insulating polymer matrices. Qiu et al. demonstrated that a blend of poly(3-hexylthiophene) (P3HT) and poly(ϵ -caprolactone) could be processed as low as $60 \text{ }^\circ\text{C}$. The organic field-effect transistors (OFETs) prepared by this method exhibited an average mobility of $1.0 \times 10^{-2} \text{ cm}^2 \text{ V}^{-1} \text{ s}^{-1}$, and an on/off current ratio of 3×10^3 .^[23] The blending approach takes advantage of phase segregation between the two incompatible polymers, leading to vertical-phase-separation or the formation of semiconducting polymer self-assembled networks in the insulating matrix polymer. This has been studied in more detail for solution-processed blends.^[24–29] The poor morphological stability is seen as a liability for such blended thin films.^[30] It needs to be pointed out there are other solventless processing methods that involve much lower temperatures or even room temperatures, such as solid–solid transfer and friction transfer.^[31–33] Different from melt-processing, these methods do not involve a reversible liquefaction–solidification process. It is often found that such solid state processing methods present a significant difficulty to control uniformity and thickness of the thin films. To face the challenges and make solventless (melting) processing a viable technology for manufacturing organic electronics, we essentially need to develop melt-processable semiconducting polymers that present both excellent electronic performance and stable thin film morphology.

In this communication, we report a general strategy to make melt-processing of semiconducting polymers attractive and practical for organic electronics, and free of the issues associated with solution-processing methods. Our approach involves complementary semiconducting polymer blends (*c*-SPBs), which are composed of a semiconducting matrix polymer with conjugation-break spacers along the polymer backbone and a fully conjugated polymer that functions as a tie chain.^[34] Such a molecular design imparts a strong interaction between matrix polymers and tie chain polymers in *c*-SPBs and efficient charge transport is a result of such an interaction, being fundamentally different from the reported blends of insulating polymers/semiconducting polymers where macroscopic phase segregation is often involved. Hence, we hypothesize it will not only make *c*-SPBs melt-processable, but also ensure a stable morphology

Dr. Y. Zhao, X. Zhao, A. Gumyusenge, Prof. J. Mei
Department of Chemistry
Purdue University
West Lafayette, IN 47907, USA
E-mail: jgmei@purdue.edu
M. Roders, Prof. A. L. Ayzner
Department of Chemistry and Biochemistry
University of California at Santa Cruz
CA 95064, USA



DOI: 10.1002/adma.201605056

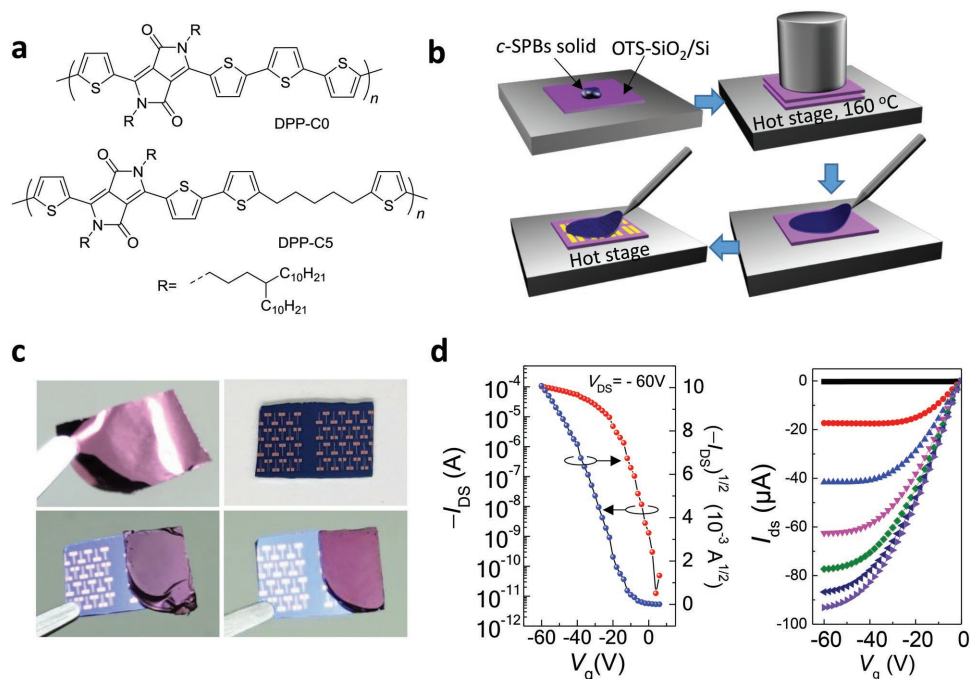


Figure 1. Materials, fabrication procedure, and OFET characterization of melt-processed devices. a) Chemical structure of DPP-C0 and DPP-C5. b) Scheme of the melt-processing approach. c) Images of a melt-processed c-SPB film and the corresponding devices using a peel-off and transfer approach. d) Representative transfer and output characteristics of melt-processed c-SPB OFETs with 60 μm channel length and 1000 μm channel width.

and excellent electronic performance for their thin films. In this study, we choose the diketopyrrolopyrrole (DPP)-based polymer DPP-C5 as a matrix polymer, together with DPP-C0 as a tie chain polymer (as shown in **Figure 1**), to verify such a hypothesis. We find that the melt-processed devices exhibit an average mobility around $0.4 \text{ cm}^2 \text{ V}^{-1} \text{ s}^{-1}$ and current on/off ratio higher than 10^5 , a record performance for melt-processed OFETs. Furthermore, in situ temperature-dependent grazing incidence X-ray diffraction (GIXRD) and charge transport measurements provide the evidence that the selected c-SPB has a reproducible thin film microstructure and device performance, which could nearly return to their original states. Such features have not been reported for any known polymer blends, while they are critical for the adoption of melt-processing as a viable technology in industrial manufacturing of organic electronics.

The pair of DPP-C5 and DPP-0 was chosen for the demonstration of melt-processing, because DPP-C5 had a relatively low melting temperature of 138 °C (Figure S1, Supporting Information) and the solution-processed c-SPB (95 wt% DPP-C5 and 5 wt% DPP-C0) showed an average charge mobility of $0.53 \text{ cm}^2 \text{ V}^{-1} \text{ s}^{-1}$.^[17] The differential scanning calorimetry (DSC) measurement of c-SPB showed a clear melting peak at 139 °C, slightly higher than the pure DPP-C5 (Figure S2, Supporting Information). Melt-processed OFETs were fabricated by a direct hot-press approach^[18] or by a hot-press and peel-off approach. For the peel-off approach, the c-SPB solid was sandwiched between two octadecyltrichlorosilane (OTS)-modified SiO₂/Si wafers on a hot plate (Figure 1b). After being heated up to 160 °C, the c-SPB solid was pressed ($\approx 10 \text{ kN cm}^{-2}$) by a heavy object. The thickness of the obtained thin films was determined to be in the range of 1–2 μm (Figure S3, Supporting Information),

which was mainly controlled by the amount of material applied, temperature, and pressing time (see the Supporting Information and Table S1 in the Supporting Information for the experimental details). Conceivably, a thin film of c-SPBs can also be obtained by an extrusion process—a continuous thin film production process widely applied in plastic industry. The film was then peeled off, transferred, and laminated onto an OTS-modified SiO₂/Si wafer with prepatterned Au-electrodes, as shown in Figure 1b,c. It was noticed that the obtained free-standing film is smooth and shows metallic luster. The laminated devices were thermally treated to ensure good contact between semiconducting thin films and electrodes/dielectrics before electrical measurements. The representative transfer and output curves of the melt-processed OFETs by both methods are shown in Figure 1d and Figure S4 (Supporting Information). The devices exhibited an average mobility around $0.4 \text{ cm}^2 \text{ V}^{-1} \text{ s}^{-1}$ and current on/off ratio higher than 10^5 . This is so far the record for melt-processed OFETs. The result is also comparable with $0.53 \text{ cm}^2 \text{ V}^{-1} \text{ s}^{-1}$ from the spin-coated OFETs performed as the control experiments. In addition, considerably smaller device-to-device variation was observed for melt-processed devices, which resulted from the uniform morphology across the thin film, as revealed by atomic force microscopy in Figure S3 (Supporting Information). Hysteresis tests were also performed to investigate whether additional defects were produced during the film transfer process. No significant difference was observed between the melt-processed and the spin-coated OFETs as shown in Figure S5 (Supporting Information).

To investigate the evolution of thin film morphology during the process of melting and cooling (crystallization), temperature-dependent, 2D GIXRD experiments were

performed. DPP-C0, DPP-C5, and the *c*-SPB thin films were deposited on OTS-modified silicon wafers by spin coating. We chose spin-coated thin films for the GIXRD experiments, instead of free-standing melt-processed films. Because they are usually thick ($\approx 1 \mu\text{m}$) and are not suitable for the GIXRD measurements to reveal the chain orientation information at the interface. Prior to GIXRD measurements, the thin films were annealed at 120°C in a glovebox (oxygen and moisture levels less than 1 ppm) to largely remove organic solvent residues and the film's thermal history. In situ temperature-dependent GIXRD experiments involved stepwise heating and cooling of the sample from room temperature to 160°C , with sufficient dwell time for thermal equilibration prior to each recorded XRD image. The in-plane and out-of-plane 2D GIXRD patterns and their corresponding 1D GIXRD curves are presented in Figure 2 and Figures S6–S8 (Supporting Information).

At 25°C , all three samples show clear edge-on molecular packing mode with π - π stacking ($0k0$) peaks appearing in the in-plane direction at $Q \approx 1.7 \text{ \AA}^{-1}$ and lamellar packing ($h00$) peaks in the out-of-plane direction beginning at $Q \approx 0.25 \text{ \AA}^{-1}$. More than four orders of Bragg reflections were observed for

all three samples, indicating that samples were highly crystalline in the vertical lamellar direction. The lamellar spacing distances were 23.53, 23.30, and 23.34 \AA for DPP-C0, DPP-C5, and *c*-SPB, respectively, while the π - π stacking distances were measured to be 3.69, 3.70, and 3.72 \AA , respectively.

Figure 2a,d,g shows out-of-plane and in-plane 2D GIXRD patterns, as well as 1D GIXRD line profiles for a DPP-C0 film. Upon heating, the lamellar packing peaks moved gradually to smaller Q vectors from 0.27 \AA^{-1} at 25°C to 0.25 \AA^{-1} at 160°C , corresponding to the d -spacing distance increasing from 23.53 to 25.13 \AA . Concomitantly, peak intensities decreased with temperature. Upon cooling, the lamellar packing distance gradually returned to 23.60 \AA at 25°C . On the other hand, the π - π stacking distance increased from 3.69 to 3.74 \AA upon heating from 25 to 160°C and returned to 3.68 \AA upon cooling back to 25°C . A clear (010) peak and a fourth-order (400) peak were present at 160°C , although at diminished intensities relative to room temperature as expected.

Figure 2b,e,h presents out-of-plane and in-plane 2D GIXRD patterns, as well as 1D GIXRD line profiles for the DPP-C5 film. DPP-C5 showed a melting temperature around 138°C with an

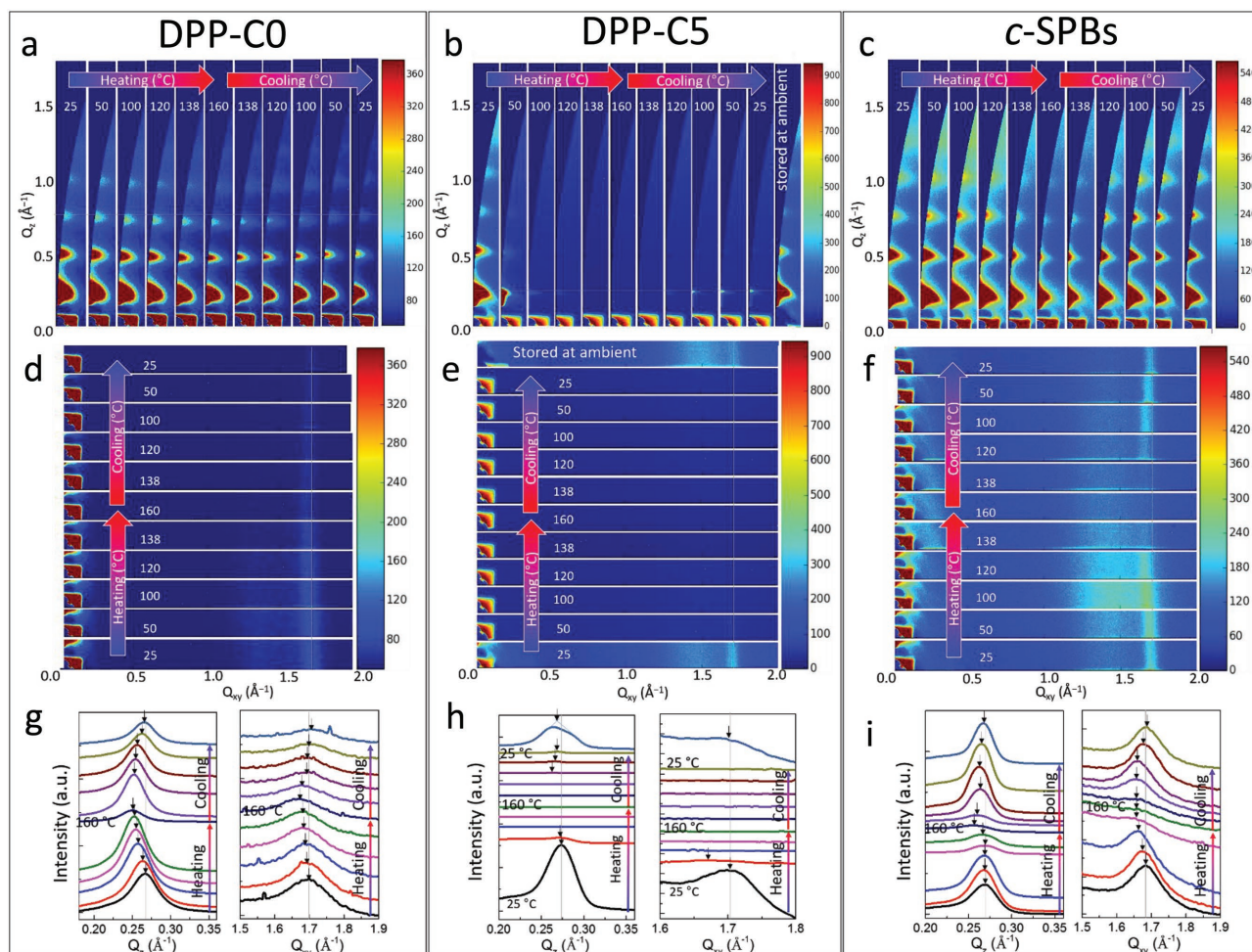


Figure 2. Temperature-dependent GIXRD results. a–c) The out-of-plane temperature-dependent 2D GIXRD patterns of DPP-C0, DPP-C5, and *c*-SPB thin films, respectively. d–f) The in-plane temperature-dependent 2D GIXRD patterns of DPP-C0, DPP-C5, and *c*-SPB thin films, respectively. g–i) Their corresponding 1D GIXRD curves. All the thin films were annealed at 120°C for 10 min in glovebox.

onset of 98 °C using DSC (Figure S1, Supporting Information). Although the bulk phase transition temperature may differ from that of the thin film state, it was still a surprising result that almost all the GIXRD peaks of the DPP-C5 thin film quickly disappeared upon heating. At 50 °C, the π - π stacking peaks were almost absent, while the higher orders of the lamellar Bragg reflection lose substantial intensity along Q_z . When the temperature was further increased to 120 °C, all diffraction peaks disappeared. It corresponded to DPP-C5 undergoing a solid-to-liquid phase transition, leading to the loss of long-range order and molecular packing motifs. Upon cooling back to 25 °C, only a weak (100) peak remained. This is in stark contrast with the DSC measurement, in which a crystallization transition was observed to occur around 100 °C. We speculated that the crystallization may take longer for the thin film. Thus, the same sample's GIXRD pattern was measured again at 25 °C after leaving the film in ambient environment for 30 d. All original diffraction peaks reemerged as shown in Figure 2b,e,h, as well as in Figure S7 (Supporting Information). In a separate study, we found out that it actually took up to 12 h (overnight) for the diffraction peaks to reemerge after melting.

Figure 2c,f,i displays out-of-plane and in-plane 2D GIXRD patterns, as well as 1D GIXRD line profiles for the *c*-SPB film (95 wt% DPP-C5 and 5 wt% DPP-C0). Compared with the pure DPP-C5 thin film, the *c*-SPB film exhibited a completely different temperature-morphology relationship. Upon elevation in temperature, the position of GIXRD π - π stacking diffraction peaks at $Q \approx 1.7 \text{ \AA}^{-1}$ moved gradually to a smaller Q , while peak widths increased and their intensities decreased at high temperatures. This corresponded to an increase in the π -stacking distance and an overall decrease in film crystallinity. Notably, both the lamellar packing and π - π stacking diffraction peaks were persistently present from room temperature to 160 °C. However, both were significantly reduced around 138 °C. This observation is in a good agreement with the DSC measurement, in which the *c*-SPB started to melt around 110 °C with a melting temperature around 139 °C (see Figure S2, Supporting Information). The presence of a clear fourth-order lamellar packing peak and a weak π - π stacking diffraction peak at 160 °C implied that the *c*-SPB preserved a significant degree of ordering even after the solid-to-liquid phase transition. As to why the *c*-SPB thin film exhibited diffraction patterns at high temperatures, it is possible that the GIXRD peaks of the *c*-SPB actually resulted from 5 wt% of DPP-C0. Since the lamellar packing and π - π stacking of DPP-C0 and the *c*-SPB are very close, it was nearly impossible to distinguish the contribution from DPP-C0 in the blend. Hence the data do not allow us to rule definitely one way or the other. With the comparable film thickness for DPP-C0 and the *c*-SPB (containing only 5 wt% DPP-C0), however, we expect that at a high temperature, the GIXRD peak intensity of DPP-C0 would be significantly stronger than the *c*-SPB, due to the lack of contribution from the majority (95 wt%) of matrix polymer DPP-C5 at high temperatures. Examining the relative intensity along the vertical direction in Figure 2, it is evident that the *c*-SPB thin film exhibits much stronger diffraction patterns instead. Therefore, the observed Bragg reflection is characteristic of *c*-SPB, and not resulting purely from DPP-C0 (5 wt%) itself. We conclude that the addition of tie chain polymer DPP-C0 to the matrix

polymer DPP-C5 helped the resulting *c*-SPB thin film to retain its packing motifs at high temperatures. Upon cooling, the diffraction pattern of the *c*-SPB gradually shifted back toward the original Q value, appearing nearly identical to the original room temperature GIXRD measurement. The in situ temperature-dependent GIXRD measurements demonstrated that crystallization of *c*-SPB is thermally reversible. The *c*-SPB showed a relatively high degree of ordering even near its melting temperature, likely due to the interactions between the tie chain polymer DPP-C0 and the matrix polymer DPP-C5.

To explore how charge transport properties of *c*-SPBs evolve with melt-processing, temperature-dependent electrical measurements were performed both in air and inside a nitrogen filled glove box. A microscope hot stage was used to precisely control the testing temperature. The heating and cooling rates were kept around 0.5 °C s⁻¹. Similarly, the thin films were thermally annealed at 120 °C before the electrical measurements and the in situ GIXRD measurements. Details of device fabrication and testing can be found in the Supporting Information. The temperature-dependent mobilities of the *c*-SPB OFETs are summarized and plotted in Figure 3.

In our previous work, we carried out temperature-dependent measurement of DPP-C0 OFETs from -148 °C (125 K) to 27 °C (300 K) under vacuum. The mobility was found to increase with temperature ($d\mu/dT > 0$) throughout the entire temperature range.^[34] In this study, the devices with DPP-C0 active layer were heated from 25 to 160 °C in air. The positive sign of $d\mu/dT$ continued when the device was heated from 25 to 75 °C, while the mobility increased slightly from 3.3 to 3.5 cm² V⁻¹ s⁻¹. When temperature was further increased, however, the sign of $d\mu/dT$ changed from positive to negative. The mobility dropped from 3.5 at 75 °C to 2.0 cm² V⁻¹ s⁻¹ at 160 °C. It is known that for OFETs that a positive $d\mu/dT$ is characteristic of charge transport via thermally activated hopping. A negative $d\mu/dT$ is often interpreted as band-like charge carrier transport (i.e., $\mu > 1.0 \text{ cm}^2 \text{ V}^{-1} \text{ s}^{-1}$). But in the current study, we do not interpret the change in sign of $d\mu/dT$ as an indication of a transition from hopping to band-like transport. Rather, we believe this turnover is a result of a competition between thermally assisted hopping and thermally induced charge carrier scattering. At relatively low temperatures (<75 °C), the contribution to charge transport from thermally charge carrier hopping is greater than thermally induced charge carrier scattering. The outcome is that $d\mu/dT$ is positive, while at high temperatures (>75 °C), thermally induced disorder and scattering become dominant. Accordingly, $d\mu/dT$ becomes negative. This hypothesis is consistent with the temperature-dependent GIXRD experiments, where the crystallinity of the thin film decreased with increasing temperature. Upon cooling, the sign of $d\mu/dT$ reversed. The transition point was still around 75 °C. Three batches of devices and more than four devices in each batch were tested, and their results were in good agreement. To avoid any complications arising from the presence of moisture and oxygen in air, and to confirm the reliability of the obtained results, the same experiment was then performed inside a nitrogen-filled glovebox. The results are shown in Figure 3d. The general mobility-temperature trend was similar, although DPP-C0 exhibiting higher charge mobilities. The sign change position was still around 75 °C. The mobility difference for the two measurements could be due to moisture and

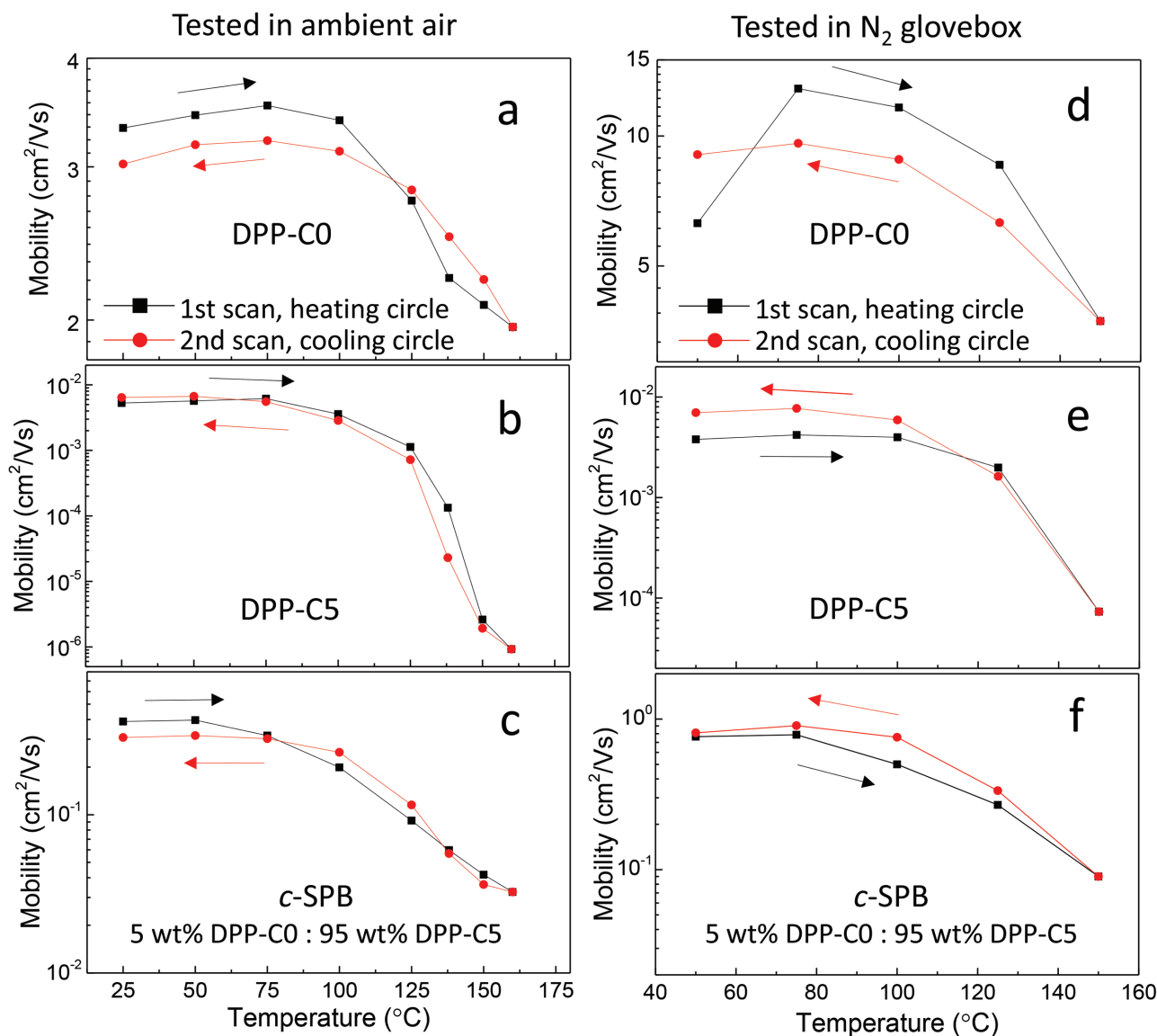


Figure 3. Temperature-dependent charge transport results. a–c) Plots of testing temperature versus the mobility measured in ambient air for OFETs using DPP-C0, DPP-C5, and c-SPB as the semiconductor, respectively. d–f) Plots produced in a nitrogen atmosphere. All tests began from the heating circle. Before measurement, all devices were annealed at 120 °C for 10 min in glovebox.

oxygen in air. A striking observation in both measurements was that DPP-C0 retained high performance with a charge carrier mobility of $2.0 \text{ cm}^2 \text{ V}^{-1} \text{ s}^{-1}$ at 160 °C both in air and in nitrogen. This may open a door for organic electronics in high temperature applications.

DPP-C5 presented several other interesting phenomena, as shown in Figure 3b. First, the mobility of DPP-C5 dramatically dropped about four orders of magnitude from $6 \times 10^{-3} \text{ cm}^2 \text{ V}^{-1} \text{ s}^{-1}$ at 75 °C to $9.3 \times 10^{-7} \text{ cm}^2 \text{ V}^{-1} \text{ s}^{-1}$ at 160 °C; while in the case of DPP-C0, it was less than half from $3.5 \text{ cm}^2 \text{ V}^{-1} \text{ s}^{-1}$ at 75 °C to $2.0 \text{ cm}^2 \text{ V}^{-1} \text{ s}^{-1}$ at 160 °C. This is likely because DPP-C5 underwent a solid-to-liquid transition in this temperature range. Second, it was also observed that its mobility of the heating circle at 138 °C was almost ten times higher than the measured mobility for the cooling circle at the

same temperature. This phenomenon can be explained by the large difference of melting and crystallization temperatures. For DPP-C5, the crystallization temperature (peak) is around 110 °C. In contrast, its melting temperature (peak) is about 138 °C.^[17] In other words, DPP-C5 behaved like a liquid at 138 °C during the cooling circle. Third, the electronic performance measured in air and in nitrogen was at the same level when it was below 120 °C, but above 138 °C the charge mobilities measured in nitrogen were about two orders of magnitude higher than those measured in air. This can be attributed to the fact that at low temperatures (below solid-to-liquid transition) the thin film of DPP-C5 retained high crystallinity, preventing the infusion of moisture or oxygen. When the temperature started getting closer to or above the melting transition, the thin film density decreased. It became easier for the moisture

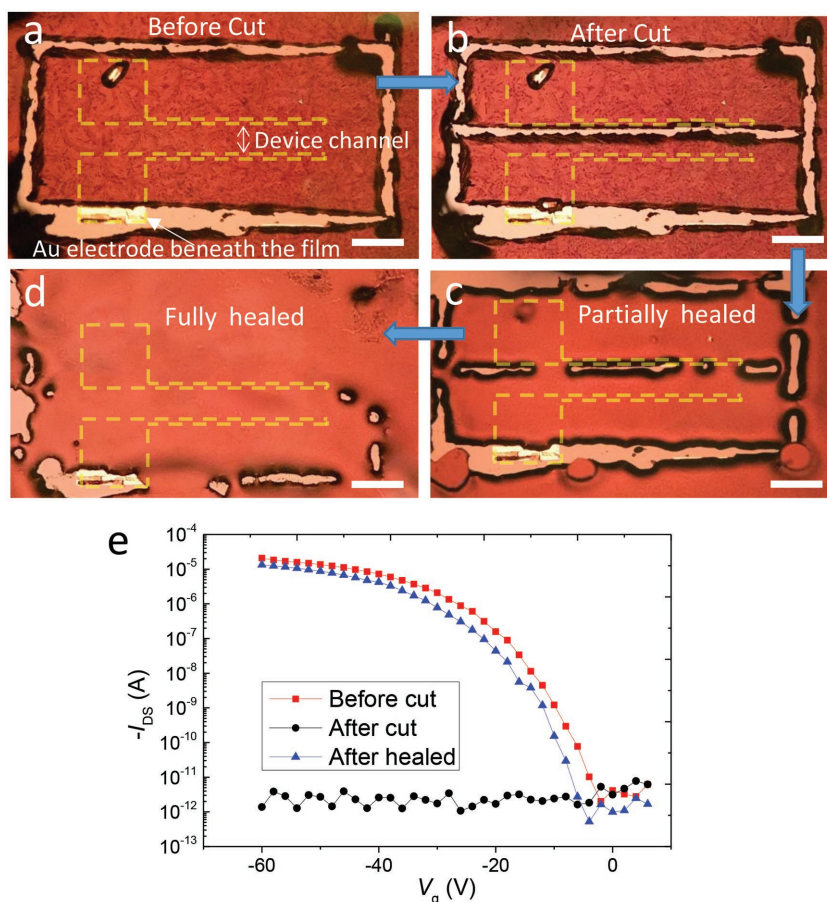


Figure 4. Reprocessability (healability) of *c*-SPB thin film field-effect transistors. a–d) Optical images of healable semiconducting polymer (scale bar is 0.2 mm). e) Electrical characterization of *c*-SPB device before cut, after cut, and after being healed.

or oxygen to diffuse into the thin film. That may have led to inferior performance in air when the measurement was carried out above the melt transition.

The *c*-SPB presented a high reversibility in the temperature-dependent electrical measurements both in air and in nitrogen between the heating and cooling cycles. The high reversibility was also observed in the GIXRD measurements as shown earlier in Figure 2c,f,i. The phenomenon of high reversibility in morphology and charge transport properties has not been reported in the previously mentioned blends of insulating (i.e., polystyrene) and semiconducting (i.e., P3HT) block copolymers.^[12] Additionally, the mobility of the *c*-SPB in air only dropped from $0.4 \text{ cm}^2 \text{ V}^{-1} \text{ s}^{-1}$ at $50 \text{ }^\circ\text{C}$ to $0.03 \text{ cm}^2 \text{ V}^{-1} \text{ s}^{-1}$ at $160 \text{ }^\circ\text{C}$, which is in stark contrast with DPP-C5. The high mobility of *c*-SPB at $160 \text{ }^\circ\text{C}$ is a reflection of the comparatively high degree of ordering in the molten *c*-SPB film, while DPP-C5 became completely amorphous as revealed by the GIXRD measurements. This observation suggests that the tie chain model, the theoretical foundation of our complementary semiconducting polymer blends,^[35] is seemingly applicable to molten thin films. Study of such an interaction in solid state and molten state is of interest in future investigations to understand charge transport in polymeric materials. The long-term stability test was also performed to evaluate the electrical properties and examine

morphological change over the course of two weeks, as displayed in Figures S13 and S14 (Supporting Information). It is clear from the measurements that the tested *c*-SPB presented excellent morphological stability and electrical performance.

To visually demonstrate the fluidity and reprocessability (healability) of *c*-SPBs, a melt-processed bottom-gate bottom-contact OFET using a blend of 95 wt% DPP-C5 and 5 wt% DPP-C0 as the semiconducting layer was fabricated. Prior to the measurement, the device was isolated by scratching a circle to avoid current leakage (Figure 4a). The device was measured in air and showed a mobility of $0.29 \text{ cm}^2 \text{ V}^{-1} \text{ s}^{-1}$ at room temperature. A notch in the channel area between source and drain electrodes of the device was then produced by a hard tungsten probe tip (Figure 4b). The source-drain current dropped to $\approx 10^{-12}$ A, a level similar to the off current level of the device (see Figure 4e). This indicated the semiconducting material was fully separated into two parts. Upon heating the device at $160 \text{ }^\circ\text{C}$ for 2 min, the semiconducting layer was partially healed as shown in Figure 4c. Full coverage of the notch was hardly achieved after an extended period of time (i.e., 30 min). This is likely due to high viscosity of the polymer melt and its poor wetting capability on OTS modified SiO_2 surface, as well as the large width of the notch ($\approx 15 \text{ }\mu\text{m}$). The optical image in Figure S15b (Supporting Information) shows that the DPP-C5 polymer melt will dewet on OTS modified SiO_2 surface

when excessive heat is provided. These two factors prevented the *c*-SPB melt from spreading on the surface and hence inhibited a quick healing of the wide notch. A small piece of OTS modified SiO_2/Si wafer was put on top of the *c*-SPB melt to facilitate the liquid flow. Upon removal of the assisting object, a fully healed channel area was obtained as shown in Figure 4d. The healed device showed a recovered charge mobility of $0.26 \text{ cm}^2 \text{ V}^{-1} \text{ s}^{-1}$. The healing process of electrical performance is illustrated in Figure 4e. This experiment was a clear demonstration of fluidity and reprocessability of *c*-SPBs as semiconductors. Even though the melting process has been used in conventional polymers for heat-triggered healing (repairing),^[36] it has been hardly demonstrated for functional semiconducting polymers. Simply, most of the high performance semiconducting polymers cannot be liquefied to flow. The demonstrated healing feature might be beneficial for future healable electronics.

To summarize, this study opens up a new pathway to melt-processable organic semiconductors through introducing complementary semiconducting polymer blends. The results demonstrate that OFETs built from these blends possess excellent morphological stability and electronic performance. A record transistor performance has been achieved via a melting process. With annual production of millions of tons of plastic

thin films (i.e., shopping bags), a great deal of information on how to apply melt-processing for producing thin films in high yields and low cost has been acquired. Much of the knowledge shall be transferrable for melt-processing of semiconducting polymer thin films. We are currently investigating continuous production of *c*-SPB thin films and electronics via a hot melt inkjet printing, while we continue to improve the electronic performance of *c*-SPBs through molecular design and understand the fluid mechanics and crystallization kinetics. In addition, we plan to investigate the potentials of *c*-SPBs for flexible electronics.

Supporting Information

Supporting Information is available from the Wiley Online Library or from the author.

Acknowledgements

The work was mainly supported by the startup fund from Purdue University and partially by the Office of Naval Research Young Investigator Program (ONR YIP), award number N00014-16-1-2551. GIXRD measurements were taken at the Stanford Synchrotron Radiation Laboratory, a national user facility operated by Stanford University on behalf of the U.S. Department of Energy, Office of Basic Energy Sciences.

Received: September 19, 2016

Revised: October 26, 2016

Published online: December 5, 2016

- [1] A. C. Grimsdale, K. L. Chan, R. E. Martin, P. G. Jokisz, A. B. Holmes, *Chem. Rev.* **2009**, *109*, 897.
- [2] J. Mei, Y. Diao, A. L. Appleton, L. Fang, Z. Bao, *J. Am. Chem. Soc.* **2013**, *135*, 6724.
- [3] A. Facchetti, *Chem. Mater.* **2011**, *23*, 733.
- [4] C. Wang, H. Dong, W. Hu, Y. Liu, D. Zhu, *Chem. Rev.* **2011**, *112*, 2208.
- [5] P. M. Beaujuge, J. R. Reynolds, *Chem. Rev.* **2010**, *110*, 268.
- [6] A. C. Arias, J. D. MacKenzie, I. McCulloch, J. Rivnay, A. Salleo, *Chem. Rev.* **2010**, *110*, 3.
- [7] I. Burgués-Ceballos, F. Machui, J. Min, T. Ameri, M. M. Voigt, Y. N. Luponosov, S. A. Ponomarenko, P. D. Lacharaise, M. Campoy-Quiles, C. J. Brabec, *Adv. Funct. Mater.* **2014**, *24*, 1449.
- [8] H. Sirringhaus, *Adv. Mater.* **2005**, *17*, 2411.
- [9] D. H. Kim, J. Mei, A. L. Ayzner, K. Schmidt, G. Giri, A. L. Appleton, M. F. Toney, Z. Bao, *Energy Environ. Sci.* **2014**, *7*, 1103.
- [10] G. Xue, J. Wu, C. Fan, S. Liu, Z. Huang, Y. Liu, B. Shan, H. L. Xin, Q. Miao, H. Chen, H. Li, *Mater. Horiz.* **2016**, *3*, 119.
- [11] G. Xue, C. Fan, J. Wu, S. Liu, Y. Liu, H. Chen, H. L. Xin, H. Li, *Mater. Horiz.* **2015**, *2*, 344.
- [12] C. Müller, C. P. Radano, P. Smith, N. Stingelin-Stutzmann, *Polymer* **2008**, *49*, 3973.
- [13] C. Müller, S. Goffri, D. W. Breiby, J. W. Andreasen, H. D. Chanzy, R. A. J. Janssen, M. M. Nielsen, C. P. Radano, H. Sirringhaus, P. Smith, N. Stingelin-Stutzmann, *Adv. Funct. Mater.* **2007**, *17*, 2674.
- [14] C. Müller, N. D. Zhigadlo, A. Kumar, M. A. Baklar, J. Karpinski, P. Smith, T. Kreouzis, N. Stingelin, *Macromolecules* **2011**, *44*, 1221.
- [15] M. A. Baklar, F. Koch, A. Kumar, E. B. Domingo, M. Campoy-Quiles, K. Feldman, L. Y. Yu, P. Wobkenberg, J. Ball, R. M. Wilson, I. McCulloch, T. Kreouzis, M. Heeney, T. Anthopoulos, P. Smith, N. Stingelin, *Adv. Mater.* **2010**, *22*, 3942.
- [16] D. Venkateshvaran, M. Nikolka, A. Sadhanala, V. Lemaur, M. Zelazny, M. Kepa, M. Hurhangee, A. J. Kronemeijer, V. Pecunia, I. Nasrallah, I. Romanov, K. Broch, I. McCulloch, D. Emin, Y. Olivier, J. Cornil, D. Beljonne, H. Sirringhaus, *Nature* **2014**, *515*, 384.
- [17] X. Zhao, Y. Zhao, Q. Ge, K. Butrouna, Y. Diao, K. R. Graham, J. Mei, *Macromolecules* **2016**, *49*, 2601.
- [18] Y. Zhao, X. Zhao, Y. Zang, C.-A. Di, Y. Diao, J. Mei, *Macromolecules* **2015**, *48*, 2048.
- [19] A. Gasperini, S. Bivaud, K. Sivula, *Chem. Sci.* **2014**, *5*, 4922.
- [20] A. Gasperini, X. A. Jeanbourquin, A. Rahmanudin, X. Yu, K. Sivula, *Adv. Mater.* **2015**, *27*, 5541.
- [21] X. Zhu, M. C. Traub, D. A. Vanden Bout, K. N. Plunkett, *Macromolecules* **2012**, *45*, 5051.
- [22] X. Xiang, W. Shao, L. Liang, X.-Q. Chen, F.-G. Zhao, Z. Lu, W. Wang, J. Li, W.-S. Li, *RSC Adv.* **2016**, *6*, 23300.
- [23] L. Qiu, Q. Xu, M. Chen, X. Wang, X. Wang, G. Zhang, *J. Mater. Chem.* **2012**, *22*, 18887.
- [24] L. Qiu, J. A. Lim, X. Wang, W. H. Lee, M. Hwang, K. Cho, *Adv. Mater.* **2008**, *20*, 1141.
- [25] G. Lu, L. Bu, S. Li, X. Yang, *Adv. Mater.* **2014**, *26*, 2359.
- [26] G. H. Lu, H. W. Tang, Y. A. Huan, S. J. Li, L. G. Li, Y. Z. Wang, X. N. Yang, *Adv. Funct. Mater.* **2010**, *20*, 1714.
- [27] S. Goffri, C. Muller, N. Stingelin-Stutzmann, D. W. Breiby, C. P. Radano, J. W. Andreasen, R. Thompson, R. A. J. Janssen, M. M. Nielsen, P. Smith, H. Sirringhaus, *Nat. Mater.* **2006**, *5*, 950.
- [28] Y. Lei, P. Deng, M. Lin, X. Zheng, F. Zhu, B. S. Ong, *Adv. Mater.* **2016**, *28*, 6887.
- [29] M. J. Ford, M. Wang, S. N. Patel, H. Phan, R. A. Segalman, T.-Q. Nguyen, G. C. Bazan, *Chem. Mater.* **2016**, *28*, 1256.
- [30] Y. Xu, J. Liu, H. Wang, Y. Han, *RSC Adv.* **2013**, *3*, 17195.
- [31] S. Nagamatsu, W. Takashima, K. Kaneto, Y. Yoshida, N. Tanigaki, K. Yase, *Appl. Phys. Lett.* **2004**, *84*, 4608.
- [32] S. Nagamatsu, W. Takashima, K. Kaneto, Y. Yoshida, N. Tanigaki, K. Yase, K. Omote, *Macromolecules* **2003**, *36*, 5252.
- [33] M. Treier, E. Orgiu, L. Zalewski, D. Cho, R. Rieger, K. Mullen, P. Samori, *J. Mater. Chem.* **2010**, *20*, 9018.
- [34] Y. Zhao, X. Zhao, M. Roders, G. Qu, Y. Diao, A. L. Ayzner, J. Mei, *Chem. Mater.* **2015**, *27*, 7164.
- [35] R. Noriega, J. Rivnay, K. Vandewal, F. P. V. Koch, N. Stingelin, P. Smith, M. F. Toney, A. Salleo, *Nat. Mater.* **2013**, *12*, 1038.
- [36] G. M. L. van Gemert, J. W. Peeters, S. H. M. Söntjens, H. M. Janssen, A. W. Bosman, *Macromol. Chem. Phys.* **2012**, *213*, 234.